Noname manuscript No.
(will be inserted by the editor)

Design and analysis of inverse tapered silicon nitride waveguide for flat and highly coherent supercontinuum generation in the mid-infrared

M. R. Karim[1], Nayem Al Kayed[2], Rakayet Rafi[3], and B. M. A. Rahman[4]

the date of receipt and acceptance should be inserted later

Abstract We numerically investigate a promising mid-infrared supercontinuum (SC) source through the design of an on-chip complementary metal oxide semiconductor compatible 3-mm-long inverse tapered waveguide made using stoichiometric silicon nitride (Si_3N_4) as the core and silica (SiO_2) glass as both the upper and lower claddings. The proposed waveguide is designed for pumping only in the anomalous dispersion regime. To explore SC generation in terms of spectral flatness and mid-infrared expansion, three different types of inverse tapered geometry are analyzed. These are inverse linear tapering, hyperbolic tapering, and parabolic tapering approaches. The proposed structures are optimized by varying their width based on the tapering variation coefficient along the pulse propagation direction. Keeping the waveguide thickness (height) constant at 2 μm, each geometry is engineered by varying widths between 1.2 μm and 0.75 μm in the mode of inverse tapering approach. Using a pump at 1.55 μm with a peak power of 8 kW, SC generation is explored in all tapering geometries with an ultrashort pulse of 50 fs. The largest SC spectra covering a region from 0.76 μm to beyond 6.67 μm have been realized with a good spectral flatness by the parabolic-type taper among the three tapering geometries considered here. To the best of the authors' knowledge, this is the first time report of broadband SC coverage through numerical study in the region of mid-infrared by Si_3N_4 planar design through a tapering approach. After spectral broadening up to 3.5 μm with a conventional uniform design, a dip has been observed at the mid of the spectra which gradually becomes large with further dimensional variations of a typical uniform waveguide. However, such spectral dip problems can largely be eliminated through selective

M. R. Karim
E-mail: mrkarim@ciu.edu.bd

[1,3]Department of Electrical and Electronic Engineering, Chittagong Independent University, Chattogram, Bangladesh

[2]Department of Physics, Engineering Physics, and Astronomy, Queens University, Canada

[4]Department of Electrical and Electronic Engineering, City University of London, UK

spectral enhancement by applying an inverse tapering approach. The coherence calculation of the predicted SC coverage also shows a highly coherent at the proposed parabolic taper output. The proposed inverse tapered planar designs show a significant improvement not only in mid-infrared spectral expansion but also in spectral flatness compared to the axially unvarying waveguide design.

Keywords Silicon nitride · Dispersion · Tapered waveguide · Integrated photonics · Supercontinuum generation

1 Introduction

In nonlinear optics, a superior optical phenomenon of generating supercontinuum (SC) spectra has lately engrossed the nonlinear optics research area due to the vivid formation of hugely broad, continuous spectra via the application of an intense, ultrashort and narrowband optical pulse into the optical waveguide [13]. The potential use of this ultra-broadband SC source in optical coherence tomography, optical frequency metrology, biomedical imaging, spectroscopy, and various industrial sensing applications [22, 42, 15] has made this kind of SC generation very popular in ultrafast optics. Moreover, the researchers are inspired to find new ideas and create novel techniques for an efficient prediction of SC through innovating compact, robust, and scalable SC light sources [37].

Over the last 10 years, low-cost, scalable integrated linear and nonlinear silicon photonics components, made-up of silicon-on-insulator (SOI) platforms, have extensively utilized complementary metal oxide semiconductor (CMOS) compatible platform by researchers [5, 44, 16, 6, 26]. In recent years, on-chip silica (SiO_2) based CMOS compatible integrated photonic devices have appeared as practical candidates for SC generation between the ultraviolet (UV) and the mid-infrared (MIR) regions [36, 12]. Expressly, in the last few years, the development of microstructured photonic crystal fiber (PCF) has led to the generation of high-brightness and broadband SC over more than three octaves [20, 8]. In the optical fiber structure, on the other hand, simple configurations such as stepwise dispersion decreasing optical fibers [1] or tapered single-mode fibers [34] are used for SC generation. Typically, SC sources (made of optical fibers) having long interaction lengths are designed which may decrease the shot-to-shot first-degree coherence of such sources [10]. To improve the coherence with short waveguide length, SC generation in chalcogenide [29], silicon [31], amorphous silicon [32], silicon nitride [21] or in III-V materials-made waveguides [11] have also been considered. Those compact millimeter waveguides have a nonlinear parameter several orders of magnitude larger than PCF, making them perfectly suitable for low-powered integrated photonic applications. In particular, SOI waveguides are promising as octave-spanning SC sources while pumped near the low two-photon absorption (TPA) window in order to avoid nonlinear loss [31]. Dispersion, pump wavelength, and peak power significantly play a vital role to determine the SC generation in the waveguide. Conveniently in a planar waveguide, SC can be predicted easily by tuning its dimensional parameters to get desired dispersion and nonlinearity at a certain wavelength but these will remain fixed across the propagation length for an uniform waveguide. Varying dispersion and nonlinearity through tapering the width of a planar waveguide

Table 1 Recent reports on SC generation using Si_3N_4 waveguide

L [mm]	λ_p [nm]	P_p [W]	Pulse duration [fs]	SC bandwidth [nm]	Study [type]	Year [Reference]
10	795	874	100	488 - 978	Exp	2015 [45]
20	1920	2000	600	1250 - 2600	Exp	2015 [40]
8	1030	4750	92	673 - 1944	Exp	2015 [21]
5.5	1064	5100	115	470 - 2130	Exp	2015 [14]
10	1555	1330	105	820 - 2250	Exp	2016 [33]
6	1556	11700	120	526 - 2600	Exp	2017 [38]
10	1550	5000	50	800 - 6500	Num	2019 [3]
2	1550	50	50	800 - 4600	Num	2020 [23]
3	1200	3800	130	400 - 1700	Exp	2020 [28]

λ_p = pump wavelength, P_p = pump peak power, Exp = Experimental, Num = Numerical

along the pulse propagation direction in lieu of keeping the waveguide uniform creates an opportunity to expand the SC bandwidth further into the mid-infrared. Selective enhancement of spectral flatness across the spectral coverage can also be observed by applying the tapering approach [24,46,41,9]. In [17,18], the authors investigated glass on silica taper waveguides, in which the dispersion profiles are modified through-thickness variation along the pulse propagation direction, however, there is fabrication complexity where the waveguide can crack with increasing height. Despite demonstrations in the optical fibers, only recently numerical studies have been reported on SC enhancement through axially varying waveguides, where the input pulse experiences varying dispersion along the propagation direction [9,18].

Stoichiometric Si_3N_4 has shown potential as a competitive material owing to higher Kerr nonlinearity than silica [21] for producing SC spectrum in the MIR. It also shows zero two-photon absorption at 1.55 μm (unlike silicon) due to a higher energy band gap (approximately 5 eV) even at high input power level in most telecommunication wavelengths and very low linear loss which can give a huge nonlinear phase shift with moderate pump power. It is transparent from ultraviolet to wavelengths beyond 6 μm in comparison with silicon [27]. On a separate note, silica goes through high material absorption in the waveguide which reduces the bandwidth of SC generation in MIR to below 3 μm [19]. Additionally, stoichiometric Si_3N_4 is highly coherent due to low Raman response, which spread throughout the SC spectrum [43]. Moreover, the material's optical properties can further be exploited for a strong nonlinear interaction by the tight light confinement through designing an on-chip integrated optical device [45,40]. Overall, to obtain spectral evolution with full spatial and temporal coherence, stoichiometric Si_3N_4 could be the more promising material for on-chip CMOS-compatible integrated photonic device fabrication for different usages in the MIR [33,38].

Recently, numerous research groups have demonstrated SC evolution between UV and MIR using Si_3N_4 uniform (axially unvarying) waveguides which are summarized in Table 1. Also, the tapered waveguide concept has recently attracted more attention. Waveguide tapering, in particular with increasing width, is shown to have a flatter and more coherent SC than a fixed dispersion waveguide when longer input pulses are used. Nevertheless, the Si_3N_4 material has not been used

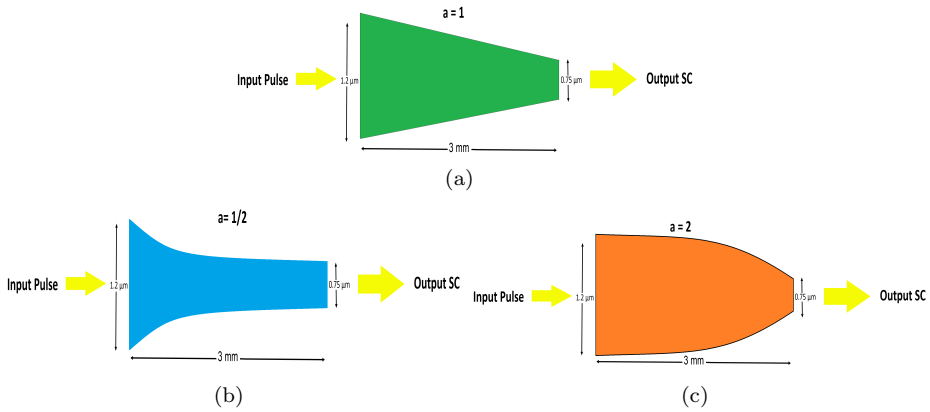

Fig. 1 Inverse tapered schematics: (a) Linear taper; b) Hyperbolic-type taper; and c) Parabolic-type tapered waveguide.

for tapering waveguides to be specific for varied tapering approaches for MIR SC generation although silica has been used for tapering approach to get a flatter and coherent SC source at the waveguide output. Furthermore, due to the strong birefringence of Si_3N_4 waveguides, broadband SC signal can be achieved by pumping either with the quasi-transverse electric (TE) or quasi-transverse magnetic (TM) mode in the anomalous dispersion regime. Such waveguides offer several advantages over optical fiber as the variation in dispersion can be controlled with greater flexibility in an integrated optics platform. The main problem with the tabulated papers' outcome is that they have got a flat SC spectrum due to the absence of solitonic propagation in the all-normal dispersion regions, which results in reduced bandwidth at the design output. Additionally, wider SC bandwidths can be predicted through anomalous dispersion pumping at the expense of an increased dip in the spectrum middle. The authors of the tabulated papers have suggested that the variation of waveguide width could help minimize the dip, which eventually reduces the SC bandwidth. On the other hand, larger SC bandwidth with more dips in the spectrum could be obtained through the variation of waveguide thickness.

In this work, a 3-mm-long planar inverse tapered design made of Si_3N_4 is proposed for SC generation in the MIR. Waveguides are tuned only for TM polarization. Three types of width-varying tapering approaches, which are optimized based on the equation developed considering different tapering variation coefficients, are rigorously discussed. Flat and highly coherent SC coverage up to 6.67 μm could be predicted by the parabolic type taper among the different tapering approaches proposed. The SC bandwidth obtained by the proposed design so far could be the largest and flatter than the bandwidth obtained by any conventional axially unvarying design.

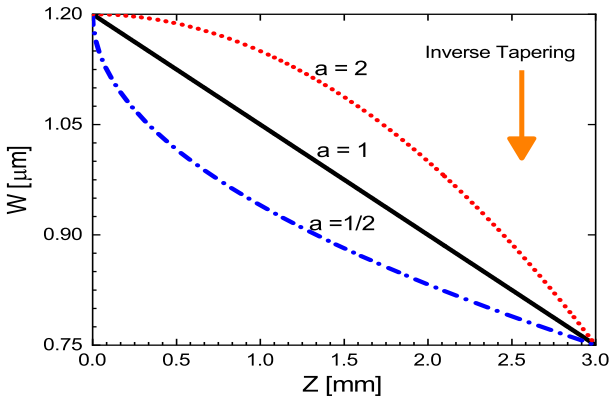

Fig. 2 Inverse tapering variations along the pulse propagation direction are based on the various values of the tapering coefficient (a).

2 Design principle

The proposed 2D schematics of Si_3N_4 are given in Fig. 1. The linear material refractive indices of the proposed design are estimated from the Sellmeier equation given in [35, 7]. We consider, in our study, an inverse tapered 3-mm-long structure with a thickness of 2 μm. The equation developed for modeling the three different types of tapering structures is

$$W(z) = W_1 - (W_1 - W_2)\left(\frac{z}{L}\right)^a \tag{1}$$

where W_1 indicates the initial width and W_2 is the final width. L is the taper length and a is the tapering variation coefficient. a can accept any values from 0 to ∞. For the proposed design, the values of a are chosen 1, 0.5, and 2 for Eq. 1 which produces linear, hyperbolic, and parabolic structures shown in Fig. 1(a), 1(b), and 1(c), respectively. W(z) indicates the width profile at position z. Variation of a induces different nonlinear pulse dynamics inside the tapering design. Figure 2 shows the W(z) profile for the inverse tapering approach with the three structural formations such as linear, hyperbolic, and exponential tapering for the various values of a mentioned above.

Previous demonstrations of SC generation in silicon waveguides have shown that most of the SC dynamics yield from the self-phase modulation, the temporal compression, and the soliton fission which induce within a few millimeters of the propagation. If one close looks at the GVD profile (which will be described in the next section), the dispersion variation can be seen between the anomalous region and all normal regions owing to the adiabatic decreasing of taper width. As all the structures have been varied by varying widths of taper in a continuous fashion, there is not at all any brief excursion from the beginning of the propagation until the waveguide end. As the GVD of the proposed waveguide relies strongly on the width, the positions of the two zero dispersion wavelengths (ZDWs), which

Table 2 Various parameter values calculated for the linear waveguide

		ZDW			At λ_p	
L [mm]	W [μm]	1st [μm]	2nd [μm]	D [ps/nm/km]	A_{eff} [μm^2]	γ [/W/km]
0	1.2	1.093	3.075	157.324	1.796	565.97
0.5	1.125	1.094	2.933	152.976	1.713	591.73
1	1.05	1.096	2.782	146.017	1.635	619.68
1.5	1.027	1.098	2.734	143.210	1.612	628.71
2	0.9	1.103	2.441	119.719	1.484	682.81
2.5	0.825	1.105	2.230	96.846	1.411	718.21
3	0.75	1.128	1.985	63.817	1.340	756.07

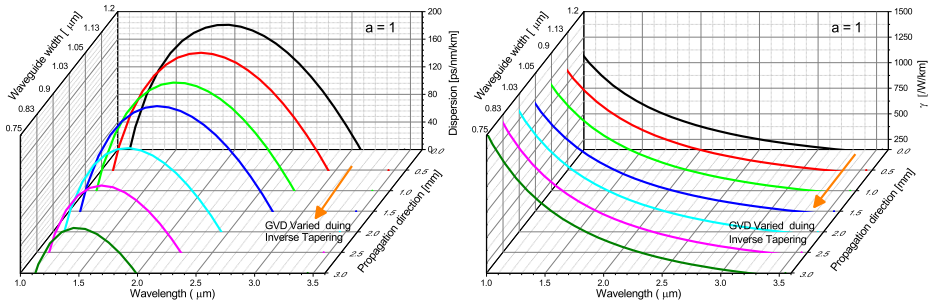

(a) (b)

Fig. 3 (a) GVD; and (b) nonlinear coefficient variations along the pulse propagation direction for the inverse linear tapering waveguide.

are crucial for the emission of DWs, are shifted towards longer wavelengths for larger-width waveguides.

COMSOL Multiphysics, the full-vectorial mode solver, is used to calculate the fundamental mode propagation constant, $\beta(\omega)$ up to the desired wavelength range [39]. The fundamental mode effective index, n_{eff} for the proposed design can then be evaluated from $\beta(\omega)$. The spatial quasi-TM mode field profiles of the fundamental mode at various wavelengths are tested and are found good confinement in the central core region which helps to produce high nonlinear interaction inside the taper. The GVD, on the other hand, another vital parameter that plays an important role in SC evolution, can be calculated from n_{eff} by using the following equation [2]:

$$\mathrm{GVD}(\lambda) = -\frac{\lambda}{c}\frac{d^2\ \mathrm{Re}(n_{eff})}{d\lambda^2} \tag{2}$$

where c indicates the speed of light.

To investigate spectral evolution in our proposed design, simulations have been performed by using an intense short-duration pulse in the waveguide anomalous GVD region by considering the generalized nonlinear Schrödinger equation (GNLSE) [25]. Due to the low Raman effect of Si_3N_4 material, the GNLSE can be solved without the Raman term and the modified form is [4]:

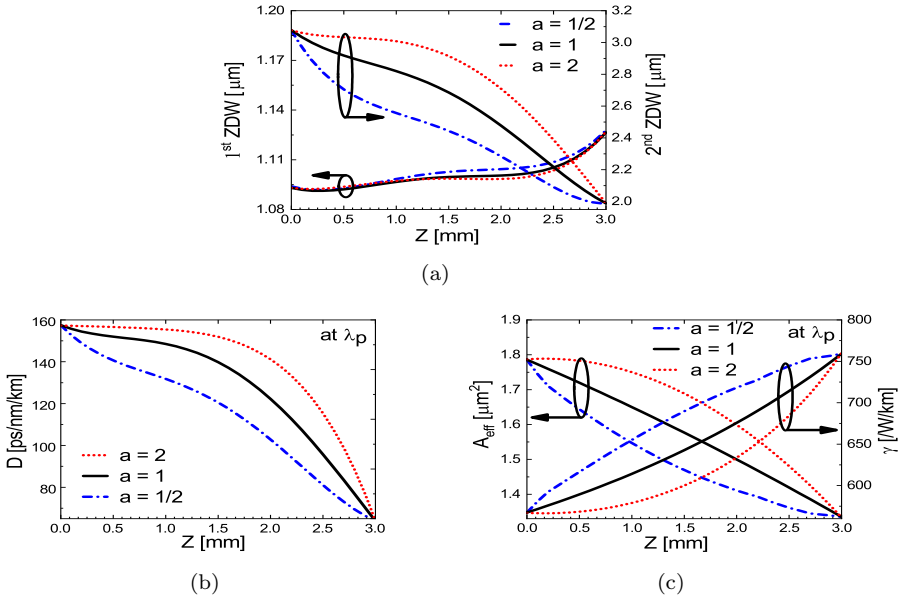

Fig. 4 Variations of (a) ZDWs; (b) GVD; and (c) A_{eff} and γ of the proposed inverse tapered waveguide for the different values of tapering coefficient along the pulse propagation direction.

$$\frac{\partial A}{\partial z} = -\frac{\alpha}{2}A + \sum_{k\geq 2}^{12} \frac{i^{k+1}}{k!}\beta_k \frac{\partial^k A}{\partial T^k} + i\gamma(|A|^2 A + \frac{i}{\omega_0}\frac{\partial}{\partial T}|A|^2 A) \tag{3}$$

where A(z,T) expresses the slowly varying pulse envelop moving at the group velocity, $v_g = 1/\beta(\omega)$ in a retarded time frame, T = t - β_1, the higher-order dispersion terms, $\beta_k$can be estimated through Taylor series from the mode propagation constant $\beta(\omega)$, the center angular frequency is expressed as ω_0 and α is the attenuation constant. The nonlinear coefficient, γ can be calculated from $n_2\omega_0/(c\mathrm{A_{eff}})$, where n_2 is the nonlinear refractive index at ω_0 and can be taken as 2.5×10^{-19} m^2W^{-1} for stoichiometric Si_3N_4 material. The wavelength, as well as z-dependent fundamental mode effective areas, are expressed by A_{eff}.

In some applications, highly coherent SC generation with large spectral bandwidth is required. The coherence of the generated SC at the output of the proposed inverse taper has thus been investigated by calculating the first-order coherence [30] and is given as

$$|g_{12}^{(1)}(\lambda)| = \frac{\langle E_1^*(\lambda)E_2(\lambda)\rangle}{\sqrt{\langle|E_1(\lambda)|^2\rangle\langle|E_2(\lambda)|^2\rangle}}. \tag{4}$$

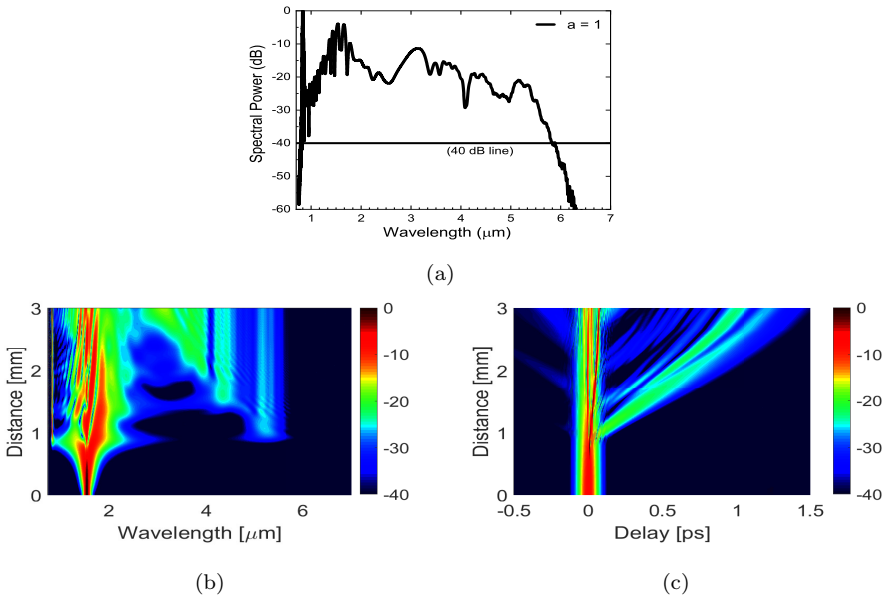

Fig. 5 SC generation at the linear tapered output: (a) Spectral coverage; (b) Density plot; and (c) Temporal plot.

where the angle brackets indicate ensemble averages over independent realizations of spectra pairs $E_{1,2}$ (λ) obtained from 100 separate simulations with different realizations of input noise [13].

3 Simulation results and analysis

To investigate the SC generation in the mid-infrared, the proposed stoichiometric Si_3N_4 waveguides are optimized using Eq. 1 with three variations viz. linear, hyperbolic, and parabolic tapering, separately. For all cases, only the width tapering mechanism is employed as the thickness tapering approach is not attractive owing to the fabrication difficulty. SC generation was also investigated for the waveguide designed using the uniform approach for comparison. All waveguides are TM polarized and are tuned for anomalous dispersion pumping at 1.55 μm wavelength.

3.1 SC generation using a linear tapering approach

SC generation is initially explored through a tapered waveguide optimized with a linearly inverse tapering approach considering the tapering variation coefficient, $a = 1$ in Eq. 1. In this approach, the waveguide is linearly tapered as shown in Fig. 1(a) by varying width between 1.2 μm to 0.75 μm. Waveguide thickness during finite-element simulations is kept constant at 2 μm. The evolution of z-dependent GVD curves (at the various width points) of the 3-mm-long tapered waveguide are illustrated in Fig. 3(a) and their corresponding evolution of nonlinear coefficient

Table 3 Various parameter values calculated for the hyperbolic waveguide

		ZDW		At λ_p		
L [mm]	W [μm]	1st [μm]	2nd [μm]	D [ps/nm/km]	A$_{eff}$ [μm^2]	γ [/W/km]
0.5	1.016	1.094	2.709	141.737	1.601	633.11
1	0.94	1.095	2.538	128.834	1.524	664.98
1.5	0.921	1.103	2.483	124.734	1.505	673.36
2	0.833	1.106	2.247	99.533	1.418	714.55
2.5	0.789	1.114	2.115	82.488	1.378	736.09

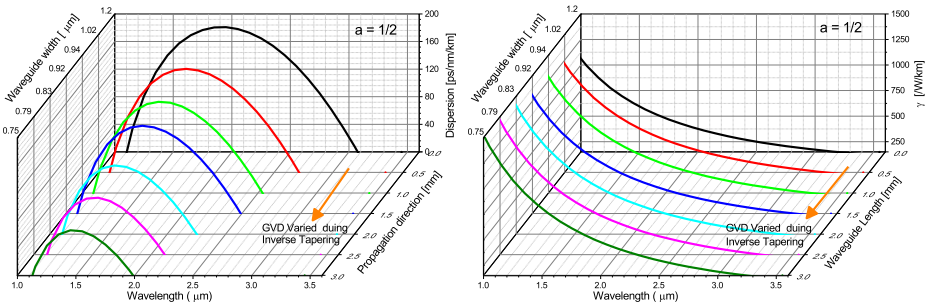

(a) (b)

Fig. 6 (a) GVD; and (b) nonlinear coefficient variations along the pulse propagation direction for the inverse tapering waveguide with the hyperbolic profile.

curves are shown in Fig. 3(b). Owing to their 3D pattern, the GVD curves are shown with anomalous dispersion region only. The variations of the GVD curve with the progression of tapering in the pulse propagation direction can be observed in Fig. 3(a). The large anomalous region with the sloppy nature of a GVD curve is observed at the starting point of a waveguide and subsequently, a reduced anomalous dispersion region is noticed as tapering progresses towards the ending point of the waveguide length. Two zero dispersion wavelengths (ZDWs) are seen on the GVD curve. The 1st ZDW is located nearly at 1.1 μm irrespective of waveguide length and the location of the 2nd ZDW is gradually shifted left from 3.1 μm to 2 μm with the axial reduction of waveguide width, which can clearly be seen from the black solid-line of Fig. 4(a). Simultaneously it is observed from Fig. 4(b) [black solid-line] that a gradual reduction of the sloppy nature of the dispersion profile as tapering progresses along the waveguide length. The z-dependent waveguide nonlinear coefficient, on the other hand, is gradually increased as the mode area reduces as shown by the black solid line in Fig. 4(c). The values of 1st and 2nd ZDWs and the values of D, A$_{\text{eff}}$, and γ at the pump wavelength (λ_{p}) for the various waveguide width (W) calculated at different tapering points (L) of the waveguide are mentioned in Table 2. Apart from tapering-induced D and γ variations, the wavelength-dependent GVD and γ are also observed in Figs. 3(a) and 3(b), respectively.

To study SC generation, numerical simulation is carried out by launching a TM polarized sech pulse of 50-fs duration (Full-Width at Half-Maximum - FWHM) into

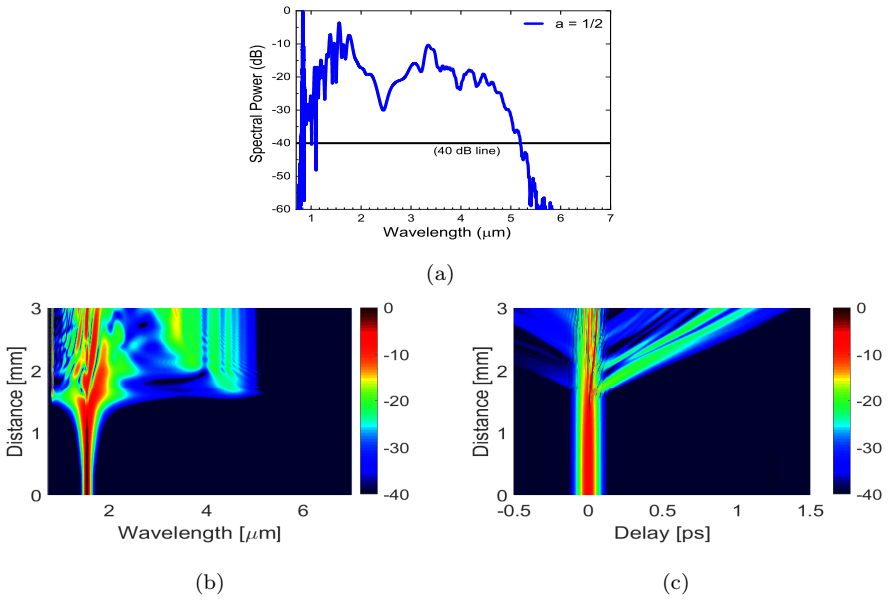

Fig. 7 SC generation at the hyperbolic tapered output: (a) Spectral coverage; (b) Density plot; and (c) Temporal plot.

the optimized waveguide with a peak power of 8 kW. The GNLSE Eq. 3 is employed for all numerical simulations. It is implemented through MATLAB software using the split-step Fourier method. 2^{17} Fourier points are used during the simulation. Linear propagation loss (α) is taken at 0.7 dB/cm during all simulations. To avoid erroneous SC generation at the waveguide output, higher-order dispersion terms up to 12th order are used. Figure 5(a) shows the SC coverage at the output of the proposed tapered waveguide and the corresponding spectral and temporal density plots are illustrated in Figs. 5(b) and 5(c), respectively. The spectral coverage can be estimated from 782 nm to 5854 nm with an approximate bandwidth (BW) of 5 μm, estimated at -40 dB from the peak. Due to a tapering mechanism applied, a significant improvement in spectral flatness is achieved over the entire output spectrum which may not be possible to obtain through designing a conventional (uniform) waveguide. For comparison, SC generation through a uniform waveguide will be analyzed and discussed in a separate section later.

3.2 SC generation by hyperbolic tapering approach

To see the impact of axial variation, SC generation is next investigated by putting the tapering variation coefficient, $a = 1/2$ in Eq. 1. In this approach, the waveguide forms a hyperbolic tapering pattern as shown in Fig. 1(b). Similar to the linear tapering approach, hyperbolic tapering is also performed by varying waveguide W between 1.2 μm and 0.75 μm keeping the waveguide H constant at 2 μm. However, the formation of the intermediate portion of this optimized waveguide is different than the linear tapering pattern owing to choosing a different value of tapering

variation coefficient, a. The GVD curves obtained for the various values of W along the waveguide length are shown in Fig. 6(a) and their corresponding nonlinear coefficient curves are depicted in Fig. 6(b). It is apparent from Fig. 6 that the D and γ vary not only with wavelength but also in pulse propagation direction as well. However, as their z-dependence shown in Fig. 4 [dash-dotted blue-lines] is different than the linear tapering waveguide proposed earlier, the values of two ZDWs, D, A_{eff}, and γ for the various intermediate width points are summarized in Table 3 (values at z = 0 and 3-mm are omitted as being same in Table 2). If we have a close look at Table 2 for the various parameter values obtained in the intermediate portion, we can see that these parameter values are different than the values obtained for the same parameters after tuning the linear tapering waveguide. The locations of both the ZDWs of GVD curves shown at various points in the pulse propagation direction followed a similar pattern to the earlier design. However, with the progression of tapering along the length the 2nd ZDW of the GVD curve, which is located in the intermediate portion of the waveguide, is shifted left with different values as can be seen from Table 3.

To explore the SC generation in the hyperbolic waveguide, simulation for SC generation is performed through GNLSE Eq. 3 by giving a similar TM polarized sech pulse as input keeping the same pulse parameters applied as before. Other simulation parameters are kept the same as applied during linear tapering waveguide simulation. The expected SC generation for the proposed hyperbolic tapering waveguide is shown in Fig. 7. The MIR spectral coverage as illustrated in Fig. 7(a) can be estimated between 760 nm and 5190 nm at a level of -40 dB from the peak. The density plots including spectral and temporal are given in Figs. 7(b) and 7(c), respectively. In this design, somewhat BW reduction is observed compared to the BW obtained from the linear tapering waveguide proposed earlier. If we compare Fig. 5(c) and Fig. 7(c), we can observe different soliton fission lengths and it may have an impact on spectral expansion at the waveguide output. In hyperbolic tapering design, soliton fission occurs after 1 mm of pulse propagation whereas soliton fission occurs before 1 mm in linear tapering design. Thus, long soliton fission length, which depends on the mode of tapering approach (i.e. for various values of a), results in rather a reduced BW at the proposed hyperbolic tapering waveguide output compared to a linear taper design.

3.3 SC generation by parabolic tapering approach

In the last two sections, SC generation is studied by considering tapering variation coefficients 1 and 1/2. After reducing the variation coefficient a from 1 to 1/2, spectral BW reduction is observed in the subsequent section. Instead of reducing a further, SC generation can next be explored by considering $a > 1$ in Eq. 1. For convenience, if we put $a = 2$ in Eq. 1, the waveguide will form a parabolic pattern as shown in Fig. 1(c). If we further increase the value of a, the waveguide will gradually become a uniform pattern where the waveguide W and H will remain the same along the length. A number of waveguides are tuned for obtaining the best results by considering the various values of $a > 1$ during parabolic tapering waveguide design. From several tuned waveguides, the best result can be obtained by the waveguide optimized with $a = 2$. The 3D pattern of GVD curves and their

Table 4 Various parameter values calculated for the parabolic structure

		ZDW			At λ_p	
L [mm]	W [μm]	1st [μm]	2nd [μm]	D [ps/nm/km]	A_{eff} [μm^2]	γ [/W/km]
0.5	1.187	1.094	3.043	156.722	1.7770	570.29
1	1.15	1.097	2.983	154.674	1.7385	582.91
1.5	1.134	1.099	2.951	153.619	1.7219	588.53
2	1	1.102	2.679	139.433	1.5844	639.61
2.5	0.887	1.103	2.401	116.337	1.4714	688.76

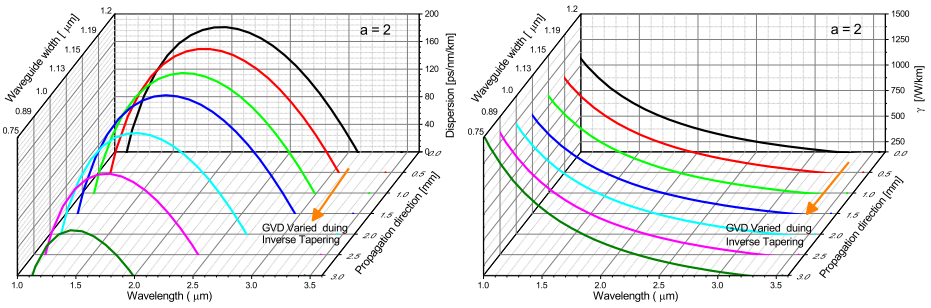

(a) (b)

Fig. 8 a) GVD; and (b) nonlinear coefficient variations along the pulse propagation direction for the inverse tapering waveguide with the parabolic profile.

corresponding nonlinear coefficient curves for the optimized parabolic tapering design are shown in Figs. 8(a) and 8(b), respectively. In this design, W varies likewise the earlier two designs while keeping H constant. Like earlier designs, two ZDWs are also found where 1st ZDW is nearly located at 1.1 μm wavelength and the 2nd ZDW is shifted left between 3 μm and 2 μm, as shown in Fig. 4(a) [dotted red-line] with the progression of parabolic tapering along the waveguide length. Certainly, the various values of ZDWs, D, A_{eff}, and γ at different points along the length in the intermediate portion of the waveguide will be different than the earlier designs due to the parabolic pattern of the waveguide and the z-dependence of these values are illustrated in Fig. 4 [dotted red-lines]. Various z-dependent parameters, shown in Table 4, are estimated at different waveguide lengths.

To see the SC generation of the parabolic waveguide, a simulation is carried out with a similar TM polarized pulse applied as before. Figure 9 shows the spectral evolution for a parabolic structure where SC coverage is estimated in the range 760 - 6675 nm with a BW of more than 5.9 μm. Two dispersive waves (DWs) owing to two ZDWs of a GVD curve are generated while the pulse propagates inside the waveguide, which clearly can be seen from the spectral density plot of Fig. 9(b). The anti stokeside DWs are induced at the same wavelength point whereas stokeside DWs are evolved at different wavelength points and are shifted gradually to the left as the pulse moves along the propagation direction. This phenomenon can clearly be observed in Fig. 9(b). Very early soliton fission occurs for this design compared to other tapering designs proposed earlier. According to

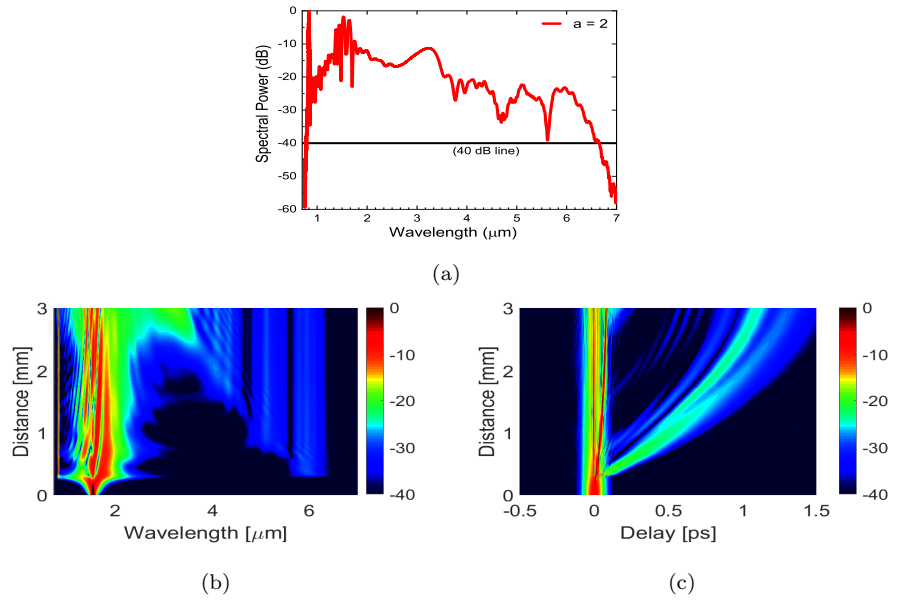

Fig. 9 SC generation at the parabolic tapered output: (a) Spectral coverage; (b) Density plot; and (c) Temporal plot.

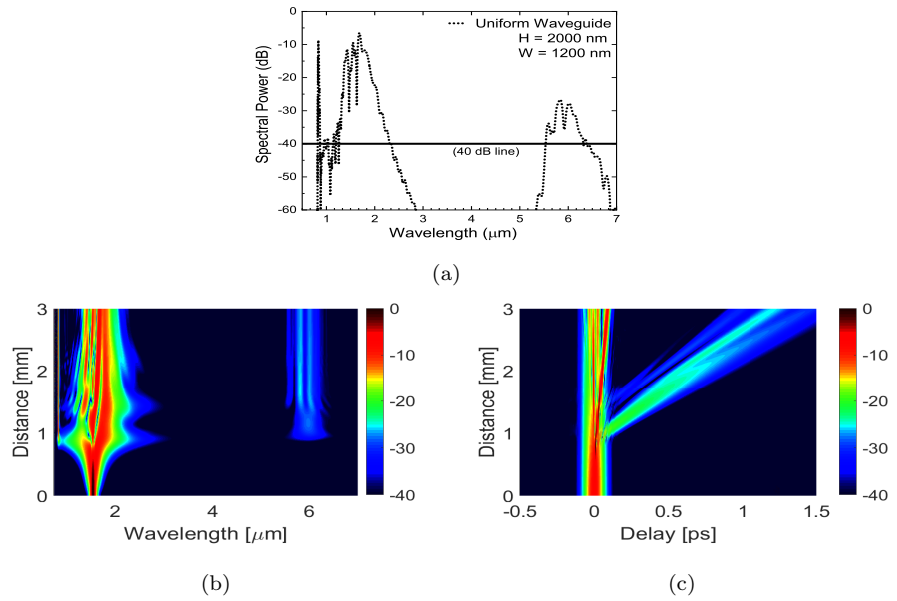

Fig. 10 SC generation: (a) Spectral coverage; (b) Density plot; and (c) Temporal plot at the uniform waveguide output maintaining waveguide $W = 1.2$ μm throughout the length.

the phenomenon explained in the previous section, the earlier fission phenomenon of parabolic taper results in a larger SC BW in comparison to the two tapering approaches discussed earlier.

3.4 SC generation using a uniform waveguide approach

To test the SC profile, spectral evolution is further investigated by varying a structure keeping its H and W constant. For this case, two terminal sections of tapered waveguide viz. $H \times W = 2\ \mu\text{m} \times 0.75\ \mu\text{m}$ and $H \times W = 2\ \mu\text{m} \times 1.2\ \mu\text{m}$ have been chosen for uniform (axially unvarying) analysis. The tailored GVD curves and their corresponding nonlinear coefficient curves are shown in Fig. 3. Actually, the starting ($H \times W = 2\ \mu\text{m} \times 1.2\ \mu\text{m}$) and final ($H \times W = 2\ \mu\text{m} \times 0.75\ \mu\text{m}$) curves represent the GVD or nonlinear coefficient curve for the corresponding design. Various parameter values: D, ZDWs, A_{eff}, and γ are shown in Table 1. Spectral coverages shown in Figs. 10 and 11 demonstrate the SC prediction at the output of 3-mm axially unvarying waveguide optimized considering input ($H \times W = 2\ \mu\text{m} \times 1.2\ \mu\text{m}$) and output terminal ($H \times W = 2\ \mu\text{m} \times 0.75\ \mu\text{m}$) of tapered waveguide separately. It can be seen from Fig. 10 that if we keep starting point (input) structure ($H \times W = 2\ \mu\text{m} \times 1.2\ \mu\text{m}$) unvarying up to the whole length of the structure, a large spectral dip in the spectrum between 2.5 μm and 5.5 μm has been observed. A separate DW centered around 6 μm is evolved in the stokeside of the spectra. On the other hand, nearly flat SC coverage can be predicted up to 3.2 μm as in Fig. 11 by a 3-mm-long unvarying endpoint structure ($H \times W = 2\ \mu\text{m} \times 0.75\ \mu\text{m}$).

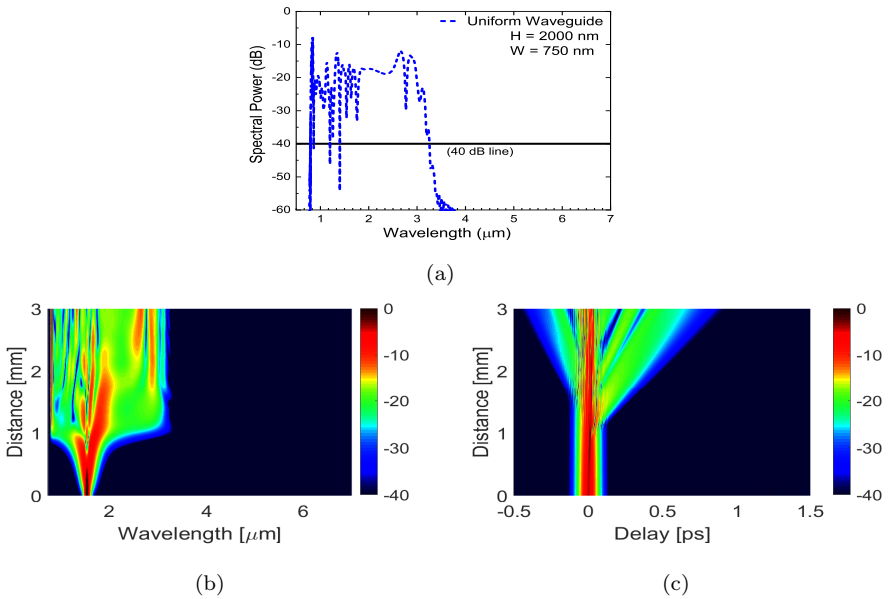

Fig. 11 SC generation: (a) Spectral coverage; (b) Density plot; and (c) Temporal plot at the uniform waveguide output maintaining waveguide $W = 750$ nm throughout the length.

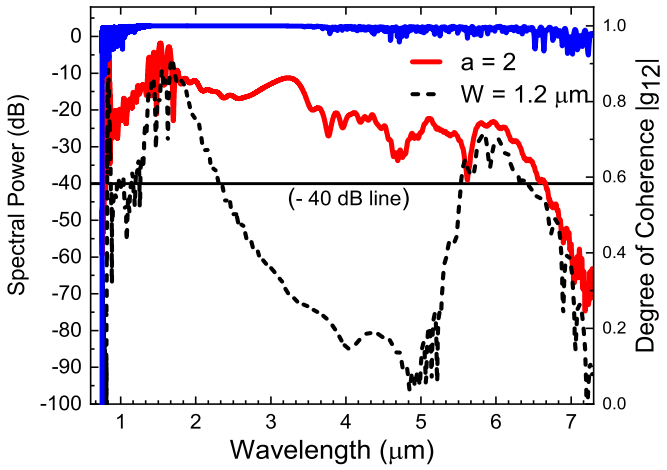

Fig. 12 SC generation comparison between conventional design (dotted black-line) and tapered design (solid red-line). The right axis shows the first degree of coherence (blue solid line on the top) for the tapered design.

3.5 Comparison and Coherence

In this section, the SC expansion profile including spectral coverage and flatness are compared between axially varying and axially unvarying designs and also spectral coherence at the output of tapered design has been tested. Comparisons are made between the spectrum of parabolic and uniform design. The spectrum for the uniform waveguide is considered only for the input point structure (($H \times W$ = 2 μm $\times$ 1.2 μm). Figure 12 depicts the comparison between two: a black dotted line and a solid red line for uniform and tapering design, respectively. It is apparent from the figure that no dip is seen over the entire spectrum and nearly flat coverage up to 6.8 μm is observed by a parabolic design. However, it is possible to obtain a flat spectrum with a reduced coverage of up to 3.2 μm by a uniform design (output point of tapered design). Therefore, we can clearly see from the above analysis that improved spectral flatness with more MIR expansion can be possible from a tapering design compared to an axially unvarying design of equal length. Finally, the first-degree coherence of 100 pairs of complex spectra of parabolic design is calculated by mixing random noise seeds with an input pulse during simulation. The degree of coherence is represented by the right axis of Fig. 12 from which unity spectral coherence (highly coherent) over the entire spectrum can be assumed with a solid blue line placed on the top. This highly coherent characteristic is more suitable for spectroscopy and optical coherence tomography in biomedical applications.

4 Conclusion

In this study, a 3-mm-long tapered Si_3N_4 planar waveguide with its three structural formations based on the different tapering coefficients has been investigated for mid-infrared SC generation. MIR spectral expansion including its flatness is thoroughly studied by tuning the proposed waveguide for a TM polarization. Proposed waveguides are simulated employing a pump at 1.55 μm. Pulse duration and peak power are used as 50-fs and 8 kW, respectively. Among the three types of inverse tapering variations considered here, initially, an inverse linear tapering approach for a waveguide design is analyzed for MIR SC generation. The numerical result shows that a MIR spectral coverage up to 5.8 μm with high spectral flatness over the entire spectra can be achieved by this design compared to the spectral coverage predicted by the waveguide designed through a uniform approach. Next, hyperbolic tapering is analyzed to investigate the MIR coverage. The SC coverage up to 5.1 μm with better spectral flatness can be obtained but somewhat less spectral BW is predicted by this design than the earlier design. By increasing the tapering variation coefficient, $a = 2$, we investigate the next tapering approach such as inverse parabolic tapering design. The simulation result for this design shows that MIR SC coverage up to 6.8 μm can be predicted to retain spectral flatness over the entire SC BW. Two axially unvarying terminal point structures have been investigated and compare their results with the tapered designs. From the analysis of three different tapered designs carried out, it is apparent that the spectral flatness as well as MIR SC expansion at the output of proposed designs have significantly improved, which may not possible by employing an axially unvarying (Uniform) design. Spectral outcome of tapered designs is tested for the first degree of spectral coherence which shows that the proposed inverse tapered waveguide is highly coherent and can be used for a variety of MIR applications such as optical sensing, biological imaging, and many more.

5 Disclosures

The authors declare no conflicts of interest.

References

1. Abrardi, L., Martín-López, S., Carrasco-Sanz, A., Corredera, P., Hernanz, M.L., González-Herráez, M.: Optimized all-fiber supercontinuum source at 1.3 μm generated in a stepwise dispersion-decreasing-fiber arrangement. Journal of Lightwave Technology **25**(8), 2098–2102 (2007)
2. Agrawal, G.P.: Nonlinear fiber optics. In: Nonlinear Science at the Dawn of the 21st Century, pp. 195–211. Springer (2000)
3. Ahmad, H., Karim, M.R., Rahman, B.M.A.: Dispersion-engineered silicon nitride waveguides for mid-infrared supercontinuum generation covering the wavelength range 0.8–6.5 μm. Laser Physics **29**(2), 025,301 (2019)
4. Al Kayed, N., Karim, M.R., Hussain, A., Jahan, N., Rahman, B.M.A.: Wideband mid-infrared supercontinuum generation using inverse tapered silicon nitride waveguide. In: 2021 IEEE International Conference on Telecommunications and Photonics (ICTP), pp. 1–5. IEEE (2021)
5. Almeida, V.R., Barrios, C.A., Panepucci, R.R., Lipson, M.: All-optical control of light on a silicon chip. Nature **431**(7012), 1081–1084 (2004)

6. Baehr-Jones, T., Pinguet, T., Guo-Qiang, P.L., Danziger, S., Prather, D., Hochberg, M.: Myths and rumours of silicon photonics. Nature Photonics **6**(4), 206–208 (2012)
7. Bass, M., Van Stryland, E.W., Williams, D.R., Wolfe, W.L.: Handbook of Optics, vol. 2. McGraw-Hill New York (1995)
8. Belli, F., Abdolvand, A., Chang, W., Travers, J.C., Russell, P.S.J.: Vacuum-ultraviolet to infrared supercontinuum in hydrogen-filled photonic crystal fiber. Optica **2**(4), 292–300 (2015)
9. Ciret, C., Gorza, S.P.: Generation of ultra-broadband coherent supercontinua in tapered and dispersion-managed silicon nanophotonic waveguides. JOSA B **34**(6), 1156–1162 (2017)
10. Corwin, K.L., Newbury, N.R., Dudley, J.M., Coen, S., Diddams, S.A., Weber, K., Windeler, R.: Fundamental noise limitations to supercontinuum generation in microstructure fiber. Physical Review Letters **90**(11), 113,904 (2003)
11. Dave, U.D., Ciret, C., Gorza, S.P., Combrie, S., De Rossi, A., Raineri, F., Roelkens, G., Kuyken, B.: Dispersive-wave-based octave-spanning supercontinuum generation in InGaP membrane waveguides on a silicon substrate. Optics Letters **40**(15), 3584–3587 (2015)
12. Duchesne, D., Peccianti, M., Lamont, M.R., Ferrera, M., Razzari, L., Légaré, F., Morandotti, R., Chu, S., Little, B.E., Moss, D.J.: Supercontinuum generation in a high index doped silica glass spiral waveguide. Optics Express **18**(2), 923–930 (2010)
13. Dudley, J.M., Genty, G., Coen, S.: Supercontinuum generation in photonic crystal fiber. Reviews of Modern Physics **78**(4), 1135 (2006)
14. Epping, J.P., Hellwig, T., Hoekman, M., Mateman, R., Leinse, A., Heideman, R.G., van Rees, A., van der Slot, P.J.M., Lee, C.J., Fallnich, C., et al.: On-chip visible-to-infrared supercontinuum generation with more than 495 thz spectral bandwidth. Optics Express **23**(15), 19,596–19,604 (2015)
15. Hartl, I., Li, X.D., Chudoba, C., Ghanta, R.K., Ko, T.H., Fujimoto, J.G., Ranka, J.K., Windeler, R.S.: Ultrahigh-resolution optical coherence tomography using continuum generation in an air–silica microstructure optical fiber. Optics Letters **26**(9), 608–610 (2001)
16. Hochberg, M., Baehr-Jones, T.: Towards fabless silicon photonics. Nature Photonics **4**(8), 492–494 (2010)
17. Hu, H., Li, W., Dutta, N.K.: Supercontinuum generation in dispersion-managed tapered-rib waveguide. Applied Optics **52**(30), 7336–7341 (2013)
18. Hu, H., Zhang, X., Li, W., Dutta, N.K.: Simulation of octave spanning mid-infrared supercontinuum generation in dispersion-varying planar waveguides. Applied Optics **54**(11), 3448–3454 (2015)
19. Hu, J., Menyuk, C.R., Shaw, L.B., Sanghera, J.S., Aggarwal, I.D.: Maximizing the bandwidth of supercontinuum generation in As_2Se_3 chalcogenide fibers. Optics Express **18**(7), 6722–6739 (2010)
20. Jiang, X., Joly, N.Y., Finger, M.A., Babic, F., Wong, G.K.L., Travers, J.C., Russell, P.S.J.: Deep-ultraviolet to mid-infrared supercontinuum generated in solid-core ZBLAN photonic crystal fibre. Nature Photonics **9**(2), 133–139 (2015)
21. Johnson, A.R., Mayer, A.S., Klenner, A., Luke, K., Lamb, E.S., Lamont, M.R.E., Joshi, C., Okawachi, Y., Wise, F.W., Lipson, M., et al.: Octave-spanning coherent supercontinuum generation in a silicon nitride waveguide. Optics Letters **40**(21), 5117–5120 (2015)
22. Jones, D.J., Diddams, S.A., Ranka, J.K., Stentz, A., Windeler, R.S., Hall, J.L., Cundiff, S.T.: Carrier-envelope phase control of femtosecond mode-locked lasers and direct optical frequency synthesis. Science **288**(5466), 635–639 (2000)
23. Karim, M.R., Al Kayed, N., Hossain, M.R., Rahman, B.M.A.: Study of low-peak-power highly coherent broadband supercontinuum generation through a dispersion-engineered si-rich silicon nitride waveguide. Applied Optics **59**(20), 5948–5956 (2020)
24. Karim, M.R., Al Kayed, N., Jahan, N., Alam, M.S., Rahman, B.M.A.: Study of highly coherent mid-infrared supercontinuum generation in cmos compatible Si-Rich SiN tapered waveguide. Journal of Lightwave Technology **40**(13), 4300–4310 (2022)
25. Karim, M.R., Rahman, B.M.A., Agrawal, G.P.: Mid-infrared supercontinuum generation using dispersion-engineered $Ge_{11.5}As_{24}Se_{64.5}$ chalcogenide channel waveguide. Optics Express **23**(5), 6903–6914 (2015)
26. Kuyken, B., Leo, F., Clemmen, S., Dave, U., Van Laer, R., Ideguchi, T., Zhao, H., Liu, X., Safioui, J., Coen, S., et al.: Nonlinear optical interactions in silicon waveguides. Nanophotonics **6**(2), 377–392 (2017)
27. Lacava, C., Stankovic, S., Khokhar, A.Z., Bucio, T.D., Gardes, F., Reed, G.T., Richardson, D.J., Petropoulos, P.: Si-rich silicon nitride for nonlinear signal processing applications. Scientific Reports **7**(1), 1–13 (2017)

28. Lafforgue, C., Guerber, S., Ramirez, J.M., Marcaud, G., Alonso-Ramos, C., Le Roux, X., Marris-Morini, D., Cassan, E., Baudot, C., Boeuf, F., et al.: Broadband supercontinuum generation in nitrogen-rich silicon nitride waveguides using a 300 mm industrial platform. Photonics Research **8**(3), 352–358 (2020)
29. Lamont, M.R.E., Luther-Davies, B., Choi, D.Y., Madden, S., Eggleton, B.J.: Supercontinuum generation in dispersion engineered highly nonlinear (γ= 10/w/m) As_2S_3 chalcogenide planar waveguide. Optics Express **16**(19), 14,938–14,944 (2008)
30. Leo, F., Gorza, S.P., Coen, S., Kuyken, B., Roelkens, G.: Coherent supercontinuum generation in a silicon photonic wire in the telecommunication wavelength range. Optics Letters **40**(1), 123–126 (2015)
31. Leo, F., Gorza, S.P., Safioui, J., Kockaert, P., Coen, S., Dave, U., Kuyken, B., Roelkens, G.: Dispersive wave emission and supercontinuum generation in a silicon wire waveguide pumped around the 1550 nm telecommunication wavelength. Optics Letters **39**(12), 3623–3626 (2014)
32. Leo, F., Safioui, J., Kuyken, B., Roelkens, G., Gorza, S.P.: Generation of coherent supercontinuum in a-Si:H waveguides: experiment and modeling based on measured dispersion profile. Optics Express **22**(23), 28,997–29,007 (2014)
33. Liu, X., Pu, M., Zhou, B., Krückel, C.J., Fülöp, A., Bache, M., et al.: Octave-spanning supercontinuum generation in a silicon-rich nitride waveguide. Optics Letters **41**(12), 2719–2722 (2016)
34. Lu, F., Knox, W.H.: Generation of a broadband continuum with high spectral coherence in tapered single-mode optical fibers. Optics Express **12**(2), 347–353 (2004)
35. Luke, K., Okawachi, Y., Lamont, M.R., Gaeta, A.L., Lipson, M.: Broadband mid-infrared frequency comb generation in a Si_3N_4 microresonator. Optics Letters **40**(21), 4823–4826 (2015)
36. Oh, D.Y., Sell, D., Lee, H., Yang, K.Y., Diddams, S.A., Vahala, K.J.: Supercontinuum generation in an on-chip silica waveguide. Optics Letters **39**(4), 1046–1048 (2014)
37. Petersen, C.R., Prtljaga, N., Farries, M., Ward, J., Napier, B., Lloyd, G.R., Nallala, J., Stone, N., Bang, O.: Mid-infrared multispectral tissue imaging using a chalcogenide fiber supercontinuum source. Optics Letters **43**(5), 999–1002 (2018)
38. Porcel, M.A., Schepers, F., Epping, J.P., Hellwig, T., Hoekman, M., Heideman, R.G., van der Slot, P.J.M., Lee, C.J., Schmidt, R., Bratschitsch, R., et al.: Two-octave spanning supercontinuum generation in stoichiometric silicon nitride waveguides pumped at telecom wavelengths. Optics Express **25**(2), 1542–1554 (2017)
39. Rahman, B.M.A., Davies, J.B.: Finite-element solution of integrated optical waveguides. Journal of Lightwave Technology **2**(5), 682–688 (1984)
40. Salem, R., Okawachi, Y., Yu, M., Lamont, M.R., Luke, K., Fendel, P., Lipson, M., Gaeta, A.L.: Octave-spanning supercontinuum generation in a silicon nitride waveguide pumped by a femtosecond fiber laser at 1.9 μm. In: CLEO: Science and Innovations, pp. STu1I–7. Optical Society of America (2015)
41. Singh, N., Vermulen, D., Ruocco, A., Li, N., Ippen, E., Kärtner, F.X., Watts, M.R.: Supercontinuum generation in varying dispersion and birefringent silicon waveguide. Optics Express **27**(22), 31,698–31,712 (2019)
42. Smirnov, S.V., Ania-Castanon, J.D., Ellingham, T.J., Kobtsev, S.M., Kukarin, S., Turitsyn, S.K.: Optical spectral broadening and supercontinuum generation in telecom applications. Optical Fiber Technology **12**(2), 122–147 (2006)
43. Wang, T., Ng, D.K.T., Ng, S.K., Toh, Y.T., Chee, A.K.L., Chen, G.F., Wang, Q., Tan, D.T.H.: Supercontinuum generation in bandgap engineered, back-end cmos compatible silicon rich nitride waveguides. Laser & Photonics Reviews **9**(5), 498–506 (2015)
44. Won, R.: Integrating silicon photonics. Nature Photonics **4**(8), 498–499 (2010)
45. Zhao, H., Kuyken, B., Clemmen, S., Leo, F., Subramanian, A., Dhakal, A., Helin, P., Severi, S., Brainis, E., Roelkens, G., et al.: Visible-to-near-infrared octave spanning supercontinuum generation in a silicon nitride waveguide. Optics Letters **40**(10), 2177–2180 (2015)
46. Zia, H., Lüpken, N.M., Hellwig, T., Fallnich, C., Boller, K.J.: Supercontinuum generation in media with sign-alternated dispersion. Laser & Photonics Reviews **14**(7), 2000,031 (2020)